UNSTEADY CFD SIMULATION OF A TURNING MID TURBINE FRAME WITH EMBEDDED DESIGN

P. Bader - W. Sanz - R. Spataro[†]

Institute for Thermal Turbomachinery and Machine Dynamics,
Graz University of Technology,
Graz, Austria,
pascal.bader@tugraz.at

ABSTRACT

This paper discusses the unsteady CFD simulation results of a new concept of an intermediate turbine duct between the high and low pressure turbine of a jet engine.
In order to meet the requirements of future jet engines it is helpful to supply the S-shaped intermediate turbine duct with struts carrying the bearing loadings. These struts can be aerodynamically optimized to generate swirl in order to replace the first vane row of the subsequent low pressure rotor.
In such a design large flow structures coming from the outlet of the transonic high pressure stage are transported towards the low pressure rotor and are superimposed by secondary flows generated by the turning struts within the duct. These effects lead to a very inhomogeneous flow reaching the downstream low pressure rotor which leads to higher losses of this rotor.
In order to reduce the fluctuations behind the S-shaped duct and to homogenize the flow, the duct can be equipped with splitters. Such an embedded design can homogenize the duct outlet flow, thus improving efficiency.
In this paper the results of a steady and unsteady CFD simulation of such a turning mid turbine frame with splitters as experimentally investigated in the transonic test turbine facility at the Institute for Thermal Turbomachinery and Machine Dynamics of Graz University of Technology are discussed. A special focus is laid on the interaction between the high pressure stage and the intermediate turbine duct and the thus induced unsteady effects. Expected differences between the steady and unsteady simulation are shown. Additionally the positive effect of the splitters on the uniformity of the flow is investigated.

NOMENCLATURE

α	Yaw angle	p_t	Total pressure
A	Stator blades	$\overline{p}$	Averaged static pressure
B_n	Number of rotor blades	$\overline{p_t}$	Averaged total pressure
C	Chord length	$\lvert\nabla p\rvert$	Pressure gradient magnitude
C_P	Pressure coefficient	$^r/_H$	Relative channel height
C_{p_t}	Total pressure coefficient	s	Entropy
$\Delta\eta$	Lost efficiency	T	Total temperature
H	Channel height	t_{step}	Time step
k	Turbulent kinetic energy	τ	Blade passing period
m	Interaction mode	$^x/_C$	Relative axial position
Ma	Mach number	y^+	Dimensionless wall distance
p	Static pressure	ω_{SW}	Streamwise vorticity

[†]Currently at Whittle Laboratory, Department of Engineering, University of Cambridge

ABBREVIATIONS

BPF	Blade passing frequency	PS	Pressure side
CFD	Computational fluid dynamics	RANS	Reynolds-averaged Navier-Stokes
HP	High pressure	SS	Suction side
ITTM	Institute for Thermal Turbomachinery and Machine Dynamics	TLV	Tip leakage vortex
		TKE	Turbulent kinetic energy
LP	Low pressure	(T)MTF	(Turning) mid turbine frame
LDV	Laser Doppler velocimetry	UPV	Upper passage vortex
LPV	Lower passage vortex	VPV	Vane passage vortex
PIV	Particle image velocimetry		

INTRODUCTION

In modern two-spool engines an S-shaped intermediate turbine duct is used to connect the high and low pressure turbine. Such a duct has a great impact on the overall performance of the engine. Therefore it is important to analyze the efficiency and the flow through this mid turbine frame (MTF). In order to reduce weight and the overall axial dimensions of an engine, it is useful to situate the bearing underneath the MTF, thus load carrying struts are necessary within the duct. These struts can also be aerodynamically optimized to generate the necessary swirl for the subsequent low pressure rotor, hence these turning struts replace the LP vane row. Such a design is called turning mid turbine frame (TMTF).

Due to the low solidity of the struts the turning of the flow is quite inhomogeneous. In addition to that, the TMTF is characterized by strong secondary flows and it transports and even enhances secondary flow structures of the upstream high pressure stage. This leads to a high rotor-rotor interaction (HP-LP rotor) and can trigger flow separation as well as vibrations at the downstream LP turbine blades. Many analyzes have been performed in the past to understand the flow through an intermediate turbine duct. Göttlich (2011) published an interesting overview of the flow features in such a duct. Also measurements and simulations were performed, e.g. Santner et al. (2011) and Lengani et al. (2012).

In order to homogenize the flow exiting the TMTF and thus the flow towards the LP rotor, splitters can be added between the struts to better guide the flow and to reduce secondary effects. Several designs were investigated in the last decade (e.g. Dominy and Kirkham (1996); Davis et al. (2002); Pullan et al. (2003); Miller et al. (2003); Marn (2008); Axelsson (2009); Lavagnoli et al. (2011)).

In this paper the design of Spataro et al. (2013a) will be investigated. This TMTF consists of 16 strut blades with two split blades embedded between two struts (32 splitters in total). A three-dimensional view of this embedded design can be found in Figure 1a. This design was developed and investigated in a transonic two-stage counter-rotating turbine rig at the Institute for Thermal Turbomachinery and Machine Dynamics (ITTM) at Graz University of Technology. For more details Hubinka et al. (2009, 2011) is recommended to the interested reader.

Previously steady (Spataro et al., 2013a) and unsteady (Spataro et al., 2013b) measurements as well as steady CFD simulations (Bader et al., 2014) have been performed to analyze the TMTF with embedded design. These publications discussed extensively the flow features through the TMTF. This paper now concentrates on the unsteady effects of the setup and the interactions of the rotor and stator blade rows.

NUMERICAL SETUP

Both steady and unsteady simulations discussed in this paper have been computed with LINARS, an in-house code which has been developed at Graz University of Technology at the ITTM (Pecnik

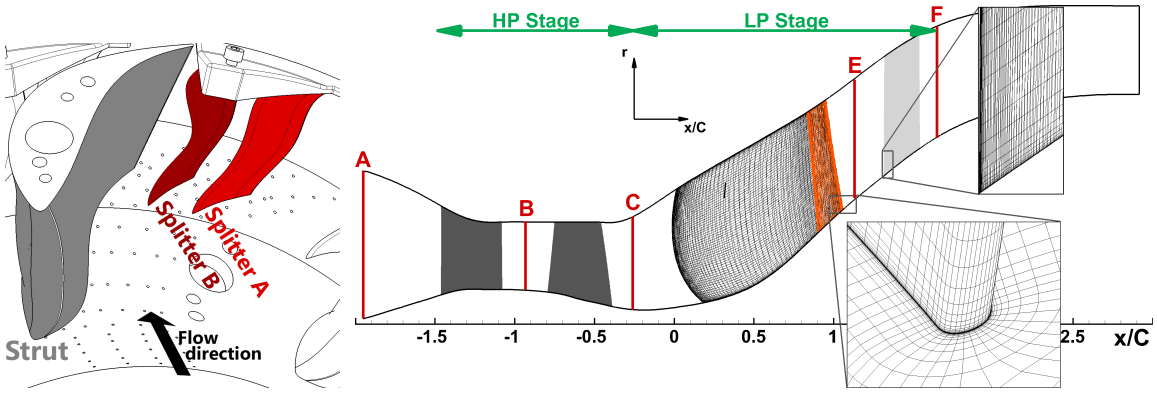

(a) **Splitter design (Spataro et al., 2013a).**

(b) **Meridional plot (Bader et al., 2014).**

Figure 1: **Sketch of the TMTF blades and the numerical setup of the TMTF.**

et al., 2005). The code solves the Reynolds-averaged Navier-Stokes (RANS) equations in conservative form with a fully-implicit, time-marching finite-volume method. The inviscid (Euler) fluxes are discretized with an upwind flux-difference splitting method of Roe (1981). As turbulence model Menter's k-ω SST model has been used (Menter, 1994).

In Figure 1b the meridional flow path through the two-stage test turbine is plotted. The turbine consists of 24 high pressure vanes, 36 unshrouded HP rotor blades, 16 strut and 32 splitter blades within the TMTF and 72 shrouded low pressure rotor blades. Extensive measurement data are available at the axi-normal planes A to F (see Fig. 1b) as well as along the sidewall and blades of the TMTF (e.g. Spataro et al. (2013a,b); Faustmann et al. (2013, 2014, 2015)).

In order to consider the circumferential periodicity, $90°$ of the whole turbine has been simulated. This results in 6 HP vanes, 9 HP rotor blades, 4 struts (with 8 splitters) and 18 LP rotor blades. The mesh consists of 228 blocks and approximately 50 million cells with y^+ lower than 1. The tip gap of the HP rotor was modeled with 34 points in radial direction.

For the steady simulation the same mesh was used, but only one flow channel of each blade row was used for the calculation which resulted in 27 blocks with a total cell number of approximately 6.3 million nodes.

Between the stationary and rotating domains a non-reflecting mixing plane was used at the interfaces for the steady simulation and a transient rotor-stator interface was used for the unsteady simulation. The endwalls were treated as adiabatic.

The time step t_{step} for the unsteady calculation was chosen in such a way, that every t_{step} the HP rotor rotates $1/30°$. After two full revolutions ($720°$) a convergent periodic solution was achieved. Data evaluation was performed for the last 2700 time steps corresponding to $90°$ rotation of the HP rotor.

The inlet of the computational domain at the very left end of Figure 1b (Plane A) was placed at a measurement plane of the test rig. Thus measurement values are available at this plane which were used as boundary conditions at the computational inlet. A uniform flow with a total pressure of 3.85 bar and a total temperature of 433.15 K as well as a uniform inlet turbulence were imposed at the inlet. The direction of the flow was set as normal-to-boundary. The turbulence level was set to 10% and the turbulence length scale to 0.001m.

The outlet at the very right end of Figure 1b (downstream of plane F) was placed at an axial distance of $(x_{out} - x_{LP_{rotor},TE})/C_{LP_{rotor}} = 6$ downstream of the low pressure rotor trailing edge. At this position a static pressure of $p_{stat} = 0.922$ bar was set at the outer endwall implying radial equilibrium.

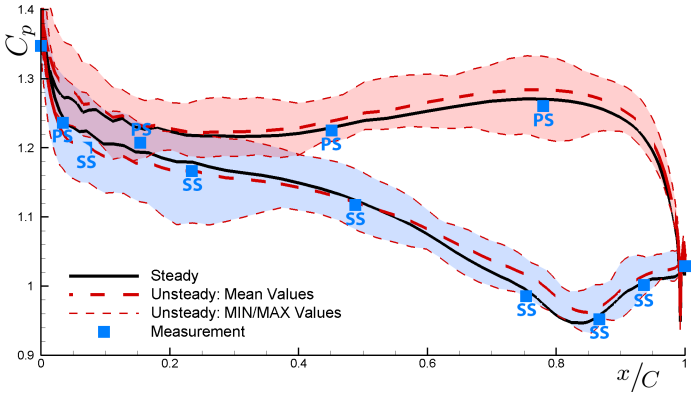

(a) **Blade loading of the TMTF strut at midspan.**

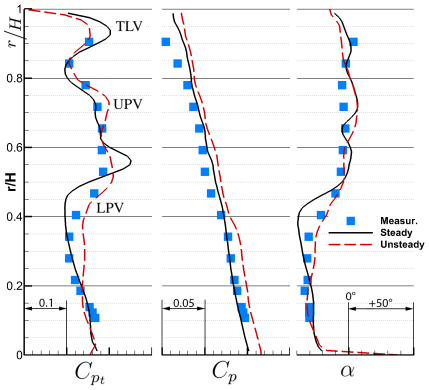

(b) **Radial distributions at plane C of the static and total pressure coefficient as well as the yaw angle.**

Figure 2: **Comparison of the steady measurement with the steady and unsteady simulations.**

VALIDATION

In order to ensure the correctness of the performed simulation the computational results were validated with measurement data.

Figure 2a shows the blade loading C_p at midspan of the strut along the relative axial position x/C. The figure shows steady measurement data as well as steady and time-averaged unsteady simulation results. Additionally the minimal and maximal pressure caused by the temporal fluctuation of the unsteady results of C_p are illustrated. The pressure coefficient C_p has been computed with

$$C_p = \frac{p - \overline{p_C}}{\overline{p_{t,C}} - \overline{p_C}} \tag{1}$$

where p represents the local static pressure and $\overline{p_C}$ and $\overline{p_{t,C}}$ the averaged static and total pressure at plane C (see Figure 1b), respectively.

In Figure 2b the radial distributions of the static and total pressure coefficient C_p and C_{p_t} as well as the yaw angle α are given. A positive α-value defines a deflection against the rotation direction of the high pressure rotor. C_{p_t} is computed similar to the static pressure coefficient (Equation 1) with

$$C_{p_t} = \frac{p_t - \overline{p_C}}{\overline{p_{t,C}} - \overline{p_C}} \tag{2}$$

Both figures show a generally good agreement between the measured and simulated results. The radial distribution of the yaw angle α of the unsteady CFD results agrees even better than the steady results which deviate especially at about 40% span where the difference to the measured value is about 15 degrees.

The mean discrepancies of α related to the mean yaw angle value in plane C are $\left|\overline{\alpha'}/\overline{\alpha_c}\right|_{steady} = 0.325\%$ and $\left|\overline{\alpha'}/\overline{\alpha_c}\right|_{unsteady} = 0.238\%$, respectively.

RESULTS AND DISCUSSION

Plane B in the HP stage

In this section the flow between the high pressure stator and rotor is analyzed. To see the unsteady effects time-space plots at plane B (between HP stator and rotor, see Fig. 1b) are given. These time-space plots are analyzed with the help of Tyler-Sofrin modes (Tyler and Sofrin, 1962). Basically Tyler and Sofrin gave a formula, which can be used to find interaction modes. The underlying theory comes from acoustics and it is also applicable for unsteady flow analysis. Thus in this paper these interaction

modes are used to describe the interactions between the HP stator and rotor blades. The modes are computed with (Tyler and Sofrin, 1962)

$$m = B_n + k \cdot A \quad \text{with k=}[-\infty, \infty] \tag{3}$$

where m represents the interaction mode, B_n represents the number of rotor blades, k the different interaction possibilities and A the number of stator blades. With the theory of Tyler and Sofrin (1962) also the rotational speed ($Spin$) of the interaction modes can be calculated with the formula

$$Spin = \frac{B_n}{m} \cdot \Omega \tag{4}$$

where Ω represents the rotational speed of the rotor. For example, if $k = 0$ is used, the result will be the blade passing frequency (BPF), which has - of course - a spin of $1\ \Omega$.

Although the number of these interaction modes is theoretically infinite ($k = \pm\infty$), experiments showed that the most important interaction modes can be found for $k = -3$ to 0, since the propagating modes are obtained with these values (see Faustmann et al. (2013, 2015)). In Table 1 these interaction modes together with their spins are listed.

Table 1: **Tyler-Sofrin interaction modes.**

k	interaction mode	spin [Ω]
-3	-36	-1
-2	-12	-3
-1	12	3
0	36	1

In the following the shock system of the transonic stage will be discussed. Therefore Figures 3 and 4 will be discussed together with Figure 5a. Figures 3 and 4 show contour plots at different time steps* of the pressure gradient in a blade-to-blade plane at 50% span and in plane B, respectively. Figure 5a shows a time-space plot of the pressure gradient $|\nabla p|$ at midspan of plane B. The ordinate shows the time and the abscissa the circumferential position. In all figures a stationary shock (strong shock) behind the HP stator is clearly visible. In Figure 3b isolines of the Mach number Ma are plotted to show the transition from super- to subsonic flow. It can also be observed that a first weak shock appears on the suction side, which is also visible in the Figures 4 and 5. The two shocks have already been found in the measurements performed by Göttlich et al. (2006) who used LDV and PIV for investigating the flow.

The dashed line in the time-space plot (Figure 5) indicates the spin of $3\ \Omega$ of the Tyler-Sofrin mode-12. Along this line zones of higher pressure gradient can be observed as small "spots". These zones are the result of a reflection of the stationary shock behind the HP stator at the rotor suction side. This reflection is illustrated in Figures 3a to c: The suction side of the rotor blade hits the shock and reflects it back towards the stator (black arrow indicates the reflection).

Since these spots are located along the mode-12 line, it can be concluded that there is an interaction of the stator and rotor. If they had come from the rotor alone the spin of the spots would have been the BPF (=1 Ω). If the mode-12 line is transferred to Figure 5b which shows the time-space plots of the turbulent kinetic energy (TKE) the effect of the shock reflection can be observed: the shock reflection can be seen as "dents" (dotted line) in the distribution of the TKE along the yellow mode-12 line. Although the distribution of the TKE shows an influence of the reflection, it does not show an increase of turbulence due to the shocks or its reflection.

Beside the mode-12 line, also the BPF (dash-dotted lines) and the wake of the stator blades (white lines) can be observed in Figure 5.

*τ represents one blade passing period.

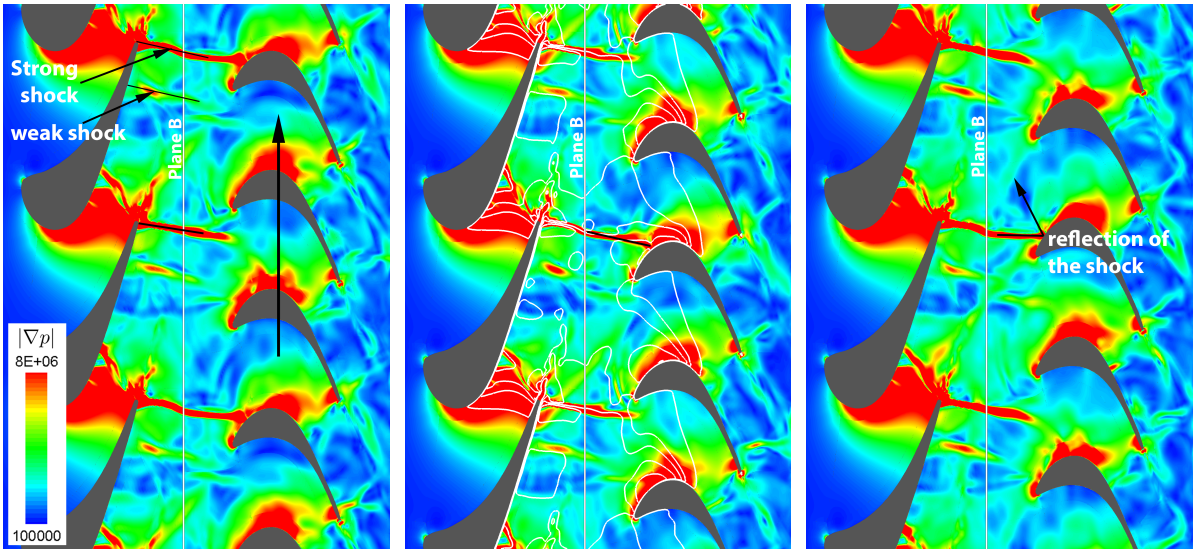

(a) $t/\tau = 0.1$. (b) $t/\tau = 0.15$ **with Ma-Isolines.** (c) $t/\tau = 0.17$.

Figure 3: **Blade-to-Blade contour plot of the pressure gradient $|\nabla p|$ at 50% span.**

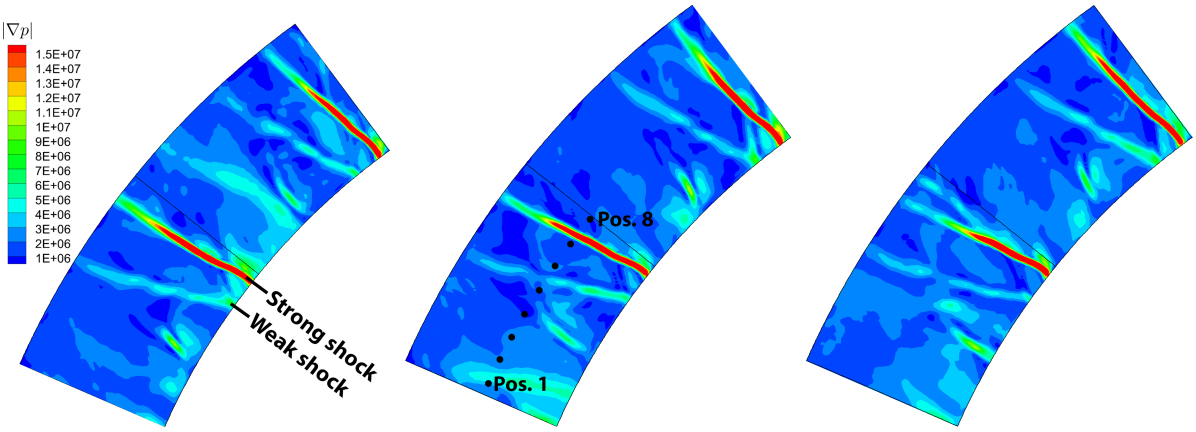

(a) $t/\tau = 0.1$. (b) $t/\tau = 0.15$. (c) $t/\tau = 0.17$.

Figure 4: **Contour plot of the pressure gradient $|\nabla p|$ at plane B - view from downstream.**

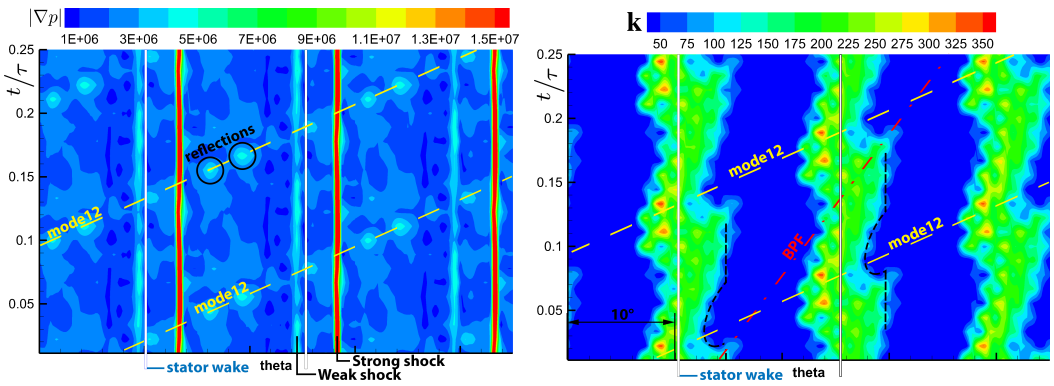

(a) **Pressure Gradient $|\nabla p|$.** (b) **Turbulent kinetic energy k.**

Figure 5: **Time-space plots at plane B at 50% span.**

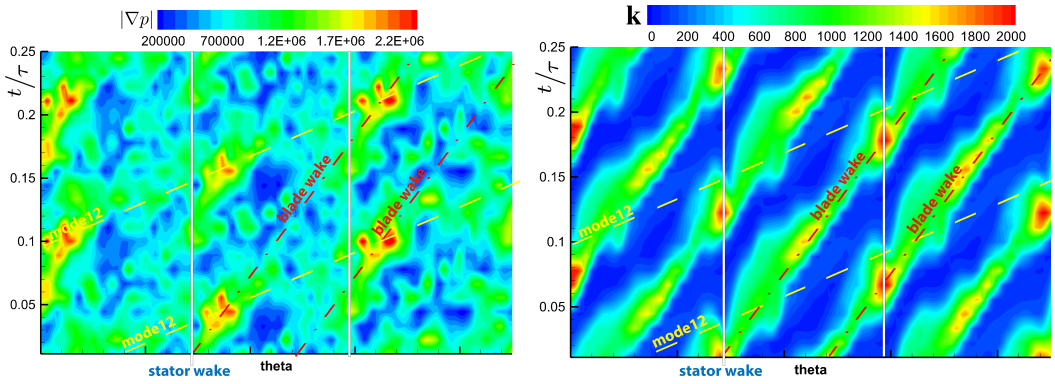

(a) **Pressure Gradient $|\nabla p|$.** (b) **Turbulent kinetic energy k.**

Figure 6: **Time-space plots at plane C at 50% span.**

Plane C downstream of the HP stage

In this section the flow downstream of the HP stage will be analyzed by studying the flow in measurement plane C located between the HP rotor and the subsequent TMTF.

With the findings discussed above, the mode-12 line can also be found in the time-space plot of plane C in Figure 6. In the time-space plot of the pressure gradient at plane C (Figure 6a) a mode-12 line again connects the zones of high pressure gradient $|\nabla p|$ similar to plane B. If the same line is drawn in the time-space plot of the TKE (Figure 6b), it does not connect zones of high TKE, but rather zones with relatively low TKE. So the shock reflections which dominate the mode-12 processes do not lead to an increase in turbulence.

The TKE time-space plot of Plane C (Figure 6b) also shows the interactions of the stator and rotor wakes, which superimpose at plane C: where the rotor and stator wakes interact, the turbulent kinetic energy plot shows a zone of higher TKE.

It can be concluded, that stator-rotor interactions influence the flow downstream of the HP stage reaching the TMTF. Not only the wake-wake interactions but also the rotor-stator interactions (reflection of the shock) are visible at the plane downstream of the HP stage. These high unsteady effects take place in the setup and need to be considered for an accurate validation of the design.

Flow within the TMTF

In order to see the influence of unsteady effects the first part of this section will discuss differences between the steady and unsteady simulation.

In Figure 2a the blade loading of the strut is given. The plot shows that the unsteady simulation agrees better with the measurement at front sections ($^x/_C \leq 0.5$) of the strut suction side while the steady simulation agrees better at aft sections ($^x/_C \geq 0.5$) of the SS. At the pressure side of the strut the measured C_P is slightly lower compared to both simulations. The steady simulation agrees slightly better with the measurements.

Additionally, the envelope of the temporal fluctuations shows, that all measured values lie within these curves. They reveal, that the SS fluctuations are higher at the front section of the strut, while the PS fluctuations are more or less constant over the chord length. This indicates stronger unsteady effects at the suction side front section. The reason for the lower fluctuations at the rear part of the suction side is that the flow experiences a high acceleration there due to the aft loading design of the strut together with the splitters placed in this part of the channel reducing the effective flow area through the strut channel.

Comparing the radial distributions at plane C (see Figure 2b) the differences between the results occur mainly at $0.2 \leq {}^r/_H \leq 0.5$ and $0.9 \leq {}^r/_H$. At ${}^r/_H \approx 0.9$ (higher p_t) the tip leakage vortex (TLV), at ${}^r/_H \approx 0.6$ (higher p_t) the upper passage vortex (UPV) and at ${}^r/_H \approx 0.35$ (lower p_t) the

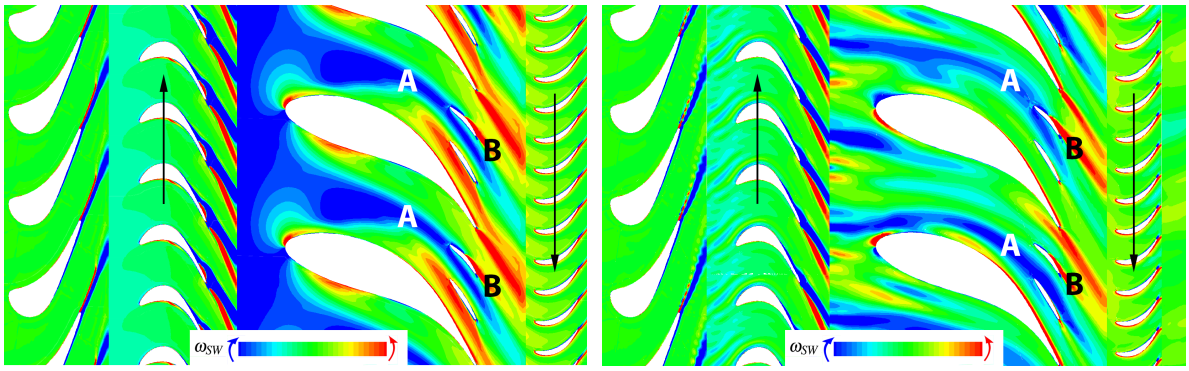

(a) **Steady simulation.** (b) **Unsteady simulation**

Figure 7: **Comparison of the streamwise vorticity ω_{SW} between steady and time-averaged unsteady simulation results at midspan.**

lower passage vortex (LPV) of the high pressure rotor can be located (Spataro et al., 2012; Bader et al., 2014).

The LPV and UPV influence the deflection of the HP rotor. Because the LPV is stronger compared to the UPV, the deflection differs in radial direction. Due to these differences in flow turning, less (UPV) respectively more (LPV) additional energy is extracted by the HP rotor which can explain a higher (UPV) respectively lower (LPV) total pressure p_t at plane C. The TLV also extracts less energy (higher p_t) due to the lack of deflection of the tip gap flow. (Spataro et al., 2012)

Comparing the two simulations, it can be observed that the total pressure close to the shroud ($^r/_H \approx 0.9$) of the steady simulation is higher compared to the unsteady simulation. This means, that less energy is extracted in the steady simulation, thus the influence of the tip gap is higher.

On the other hand the effect of the LPV computed by the steady simulation is stronger compared to the unsteady simulation. This can be observed in the radial distribution of p_t as well as in the yaw angle-distribution at $^r/_H \approx 0.35$. It seems that unsteady effects coming from the HP stage which are not considered in the steady simulation (due to the mixing plane) reduce the influence of the LPV and reduces the energy extracted at this part of the channel. These differences can also be observed in Figure 7 which shows the contour plots of the streamwise vorticity ω_{SW} at midspan for the steady and unsteady simulations. The streamwise vorticity ω_{SW} is calculated with

$$\omega_{SW} = \frac{v_x \cdot \omega_x + v_y \cdot \omega_y + v_z \cdot \omega_z}{|v|} \tag{5}$$

where v represents the velocity and ω represents the vorticity. The unsteady contour plot in Figure 7 shows time-averaged results.

The structure indicated with A represents the lower passage vortex coming from the upstream HP stage (see Bader et al. (2014)). Clearly this structure has a higher intensity in the steady case which agrees with the observations from the radial distributions given in Figure 2b.

The time-averaged unsteady contour plot also shows differences in intensity and placement of structure A between two neighboring strut channels. Due to the non-integer ratio of the HP stator and TMTF blades, the differences between the channels are caused by different clocking positions of the HP stator blades. This difference does not only influence structure A but also the flow at the splitters (e.g. indicated with B). Latter structures are reaching the LP rotor and can influence its performance due to the non-homogeneity of the flow. So the unsteady simulation shows that the high pressure stator influences the performance of the low pressure rotor, an effect not predicted by the steady simulation.

In order to analyze the flow through the TMTF more detailed, a meridional planeh as been placed within the channel as shown in Figure 8a. The Mach number at midspan of this plane is plotted in a

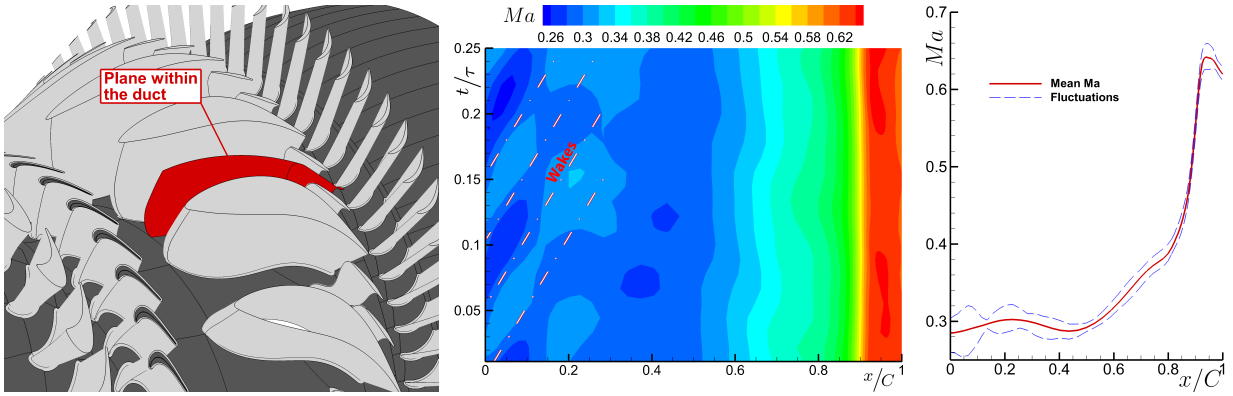

(a) **Position of the plane.**

(b) **Time-space plot within the TMTF duct of Ma at midspan.**

(c) **Streamwise distribution of Ma at midspan.**

Figure 8: **Meridional Plane within the TMTF duct.**

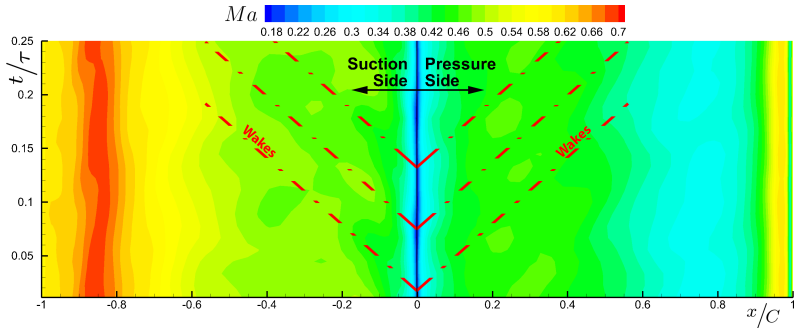

Figure 9: **Time-space plot close to the suction and pressure side of the strut blade at 50% span, showing Ma outside the boundary layer.**

time-space plot in Figure 8b. Clearly the wakes coming into the channel are visible and are indicated by dash-dotted lines. Downstream of approximately $x/C > 0.45$ the unsteady fluctuations are low and the wakes of the HP rotor are not observable anymore. The temporal fluctuations are even lower after $x/C > 0.85$ where the splitters are located. The splitters seem to have a positive effect on the temporal fluctuations. In Figure 8c the time-averaged Mach number together with the fluctuation envelope is given for the same line in the flow channel confirming the statement above.

The streamwise decrease of the fluctuations is also visible in Figure 9 which is a time-space plot of the Mach number on the suction and pressure side of the strut blade at midspan. The same conclusion can be drawn here: while wakes are visible close to the leading edge of the strut (again indicated with dash-dotted lines), the unsteady effects are decaying downstream. Also the statement made above that the SS fluctuations are higher compared to the PS fluctuations can be verified by this plot.

In summary, the splitters do not only homogenize the flow in circumferential directions as shown by Bader et al. (2014), but also may reduce the temporal fluctuations which is discussed in more detail in the following section.

Plane E downstream of the TMTF

In this section the flow reaching the downstream LP rotor will be analyzed in order to see if there is a positive effect of the splitters on the fluctuations in the flow reaching the LP rotor.

Figure 10 shows the time-space plot of the Mach number at midspan of plane E. In the plot the wakes of the strut (dashed line) and the splitters A and B (dotted lines) are plotted. The plot shows that the temporal fluctuations are quite small as already discussed above. Comparing the three channels (strut-splitter, splitter-splitter and splitter-strut) it can be observed that the circumferential fluctuations

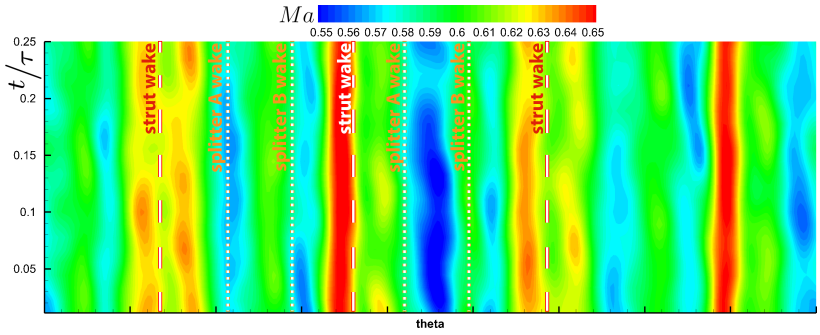

Figure 10: **Time-space plot of the Mach number at 50% span in plane E.**

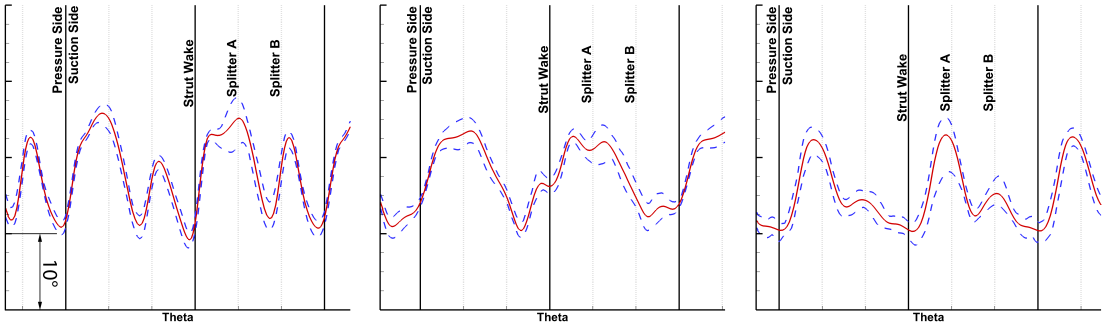

(a) **At 25% span.** (b) **At 50% span.** (c) **At 75% span.**

Figure 11: **Circumferential distribution of yaw angle α at different span positions.**

are higher than the temporal fluctuations.

Additionally, the differences between two neighboring strut channels are visible (see also Figure 7). As already mentioned, these differences are caused by the HP stator flow.

To see the flow angle of the flow entering the low pressure rotor, Figure 11 shows the circumferential distribution of the yaw angle α at 25%, 50% and 75% span. The plots show the time-averaged values together with the envelope of the fluctuations. A similar diagram has already been used by Bader et al. (2014) to show the homogenization of the circumferential fluctuations due to the splitters.

When analyzing the circumferential distribution at 25% span (Figure 11a) an interesting difference can be detected between the wakes of splitter A of the two different duct channels: there are differences of the mean value but even larger variations in temporal fluctuations. Especially the right channel shows large fluctuations. As already mentioned these deviations are caused by the HP stator which obviously has an influence on the flow reaching the LP rotor.

The midspan distribution of the yaw angle in Figure 11b again shows differences between the two channels. In the right section of the duct differences between the mean values can be observed. In the right channel there are larger yaw angles as well as larger temporal fluctuations.

At 75% span the differences of the time-averaged values are quite low between the strut channels, but the differences of the temporal fluctuations are high. Again they are strongest in the wake of splitter A.

Looking at all three charts in Figure 11 it can be generally said, that the temporal fluctuations are very low compared to the circumferential fluctuations, but local as well as temporal differences are influenced by the HP stator.

Efficiency of the turbine

As a next step the overall performance predicted by the steady and unsteady simulation is compared. Figure 12 shows the lost efficiency through the different blade rows of the turbine. The losses

were normalized with the total loss of the steady simulation. It was computed with following formula (Pullan et al., 2006)

$$\Delta\eta = \frac{\Delta s \cdot T_F}{c_p \cdot (T_A - T_F) + \Delta s_{AF} \cdot T_F} \tag{6}$$

where Δs represents the change of mass-averaged entropy through the analyzed stage evaluated at the measurement planes, Δs_{AF} through the whole turbine (from plane A to F) and T_A and T_F represent the mass-averaged total temperature at plane A and F, receptively. Every time-step of the unsteady results have first been mass-averaged and then the time-averaged result has been computed. The numbers show the relative differences in the losses for the different blade rows. The TMTF loss clearly shows the highest difference. Between the steady and unsteady simulation this can be explained by the mixing losses of the wakes and vortices which are only considered in the unsteady simulation. The steady simulation averages such flow structures circumferentially at the mixing plane interface, so that no circumferential mixing occurs downstream of the interface.

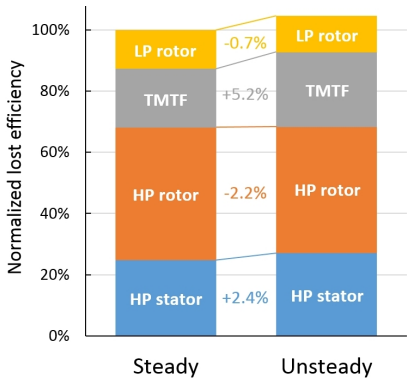

Figure 12: **Lost efficiency normalized by steady results.**

Through the rotors the lost efficiency of the unsteady simulation is smaller compared to the steady simulation. It is interesting that the HP stator has higher losses in the unsteady case despite the same steady inlet conditions at plane A. A possible reason is that the unsteady simulation considers an upstream effect of the HP rotor and stronger interactions between stator and rotor.

Also the TMTF has higher losses in the unsteady case. This is most likely caused by the unsteady wakes of the HP stage reaching the subsequent duct.

CONCLUSIONS

In this paper the results of an unsteady CFD simulation of the flow through two turbine stages containing a TMTF with embedded design are discussed. The design of the TMTF represents a promising solution to reduce weight and size of today's aero engines. An additional steady simulation has been done to better highlight the unsteady flow phenomena.

A strong rotor-stator interaction takes place in the high pressure stage which influences the flow in the succeeding TMTF. It was also found that the unsteady effects emerging from the HP stage also effect the low pressure rotor behind the TMTF and have to be considered for performance evaluations.

The yaw angle behind the TMTF shows differences in the circumferential distribution between two neighboring strut flow channels caused by clocking effects. Additionally the amplitude of the temporal fluctuations differs.

When comparing the steady and unsteady simulation results deviations are mainly caused by the mixing plane approach at the interfaces. The main differences were found in the lower passage vortex and the tip gap flow of the HP rotor as well as in the TMTF between neighboring flow channels.

The setup successfully homogenizes the flow circumferentially and also most likely temporally, which should have a positive effect on the overall performance of the low pressure turbine. Therefore

the present paper together with the work of Spataro et al. (2013a,b); Bader et al. (2014) shows that the splitter design is a promising design for future jet engines.

ACKNOWLEDGEMENTS

The research leading to these results has been partially funded by the European Union within the EU-project DREAM (contract No. ACP7-GA-2008-211861) as well as from the Austrian Federal Ministry for Finance.

The authors would also like to thank the Austrian Federal Ministry for Transport, Innovation and Technology who funded the project RELAM within the Austrian Aeronautics Program TAKE OFF.

REFERENCES

L. U. Axelsson. Experimental investigation of the flow field in an aggressive intermediate turbine duct. *PhD thesis, Department of Applied Mechanics of Chalmers University of Technology*, 2009. ISBN 0:978-91-7385-264-7.

P. Bader, W. Sanz, R. Spataro, and E. Göttlich. Flow evolution through a turning mid turbine frame with embedded design. *Proceedings of ASME 2014 TURBO EXPO, Düsseldorf, Germany*, 2014. GT2014-25009.

R. L. Davis, J. Yao, J. P. Clark, G. Stetson, J. J. Alonso, A. Jameson, C. W. Haldeman, and M. G. Dunn. Unsteady interaction between a transonic turbine stage and downstream components. *In Proceedings of ASME Turbo Expo 2002, June 3-6, Amsterdam, Netherlands*, 2002. GT2002-30364.

R. G. Dominy and D. A. Kirkham. The influence of blade wakes on the performance of inter-turbine diffusers. *Journal of Turbomachinery, 118, January, pp. 347-352*, 1996.

C. Faustmann, D. Lengani, R. Spataro, A. Marn, E. Göttlich, and F. Heitmeir. Experimental investigation of the noise generation and propagation for different turning mid turbine frame setups in a two–stage two–spool test turbine. *Proceedings of ASME 2013 TURBO EXPO, San Antonio, Texas, USA*, 2013. GT2013-95698.

C. Faustmann, S. Zerobin, A. Marn, M. Spitalny, D. Broszat, and E. Göttlich. Noise generation and propagation for different turning mid turbine frame setups in a two shaft test turbine. *20^{th} AIAA/CEAS Aeroacoustic Conference, Atlanta, GA, USA*, 2014. Paper No. 1888811.

C. Faustmann, S. Zerobin, R. Spataro, A. Marn, F. Heitmeir, and E. Göttlich. On the acoustics of a turning mid turbine frame with embedded design in a two-stage test turbine. *In Proceedings of the 11^{th} European Turbomachinery Conference 2015 Madrid, Spain*, 2015. ETC2015-137.

E. Göttlich. Research on the aerodynamics of intermediate turbine diffusers. *Progress in Aerospace Sciences 47. pp. 249–279*, 2011.

E. Göttlich, J. Woisetschläger, P. Pieringer, B. Hampl, and F. Heitmeir. Investigation of vortex shedding and wake-wake interaction in a transonic turbine stage using laser-doppler-velocimetry and particle-image-velocimetry. *Journal of Turbomachinery. 2006. Vol. 128(1). pp. 178–187*, 2006.

J. Hubinka, C. Santner, B. Paradiso, F. Malzacher, and E. Göttlich. Design and construction of a two shaft test turbine for investigation of mid turbine frame flows. *Proceedings of ISABE 2009, Montreal, Quebec, Canada*, 2009. ISABE-2009-1293.

J. Hubinka, B. Paradiso, C. Santner, H. P. Pirker, and E. Göttlich. Design and operation of a two spool high pressure test turbine facility. *Proceeding of the 9^{th} European Turbomachinery Conference conference, Istanbul, Turkey, pp 1531-1540*, 2011.

S. Lavagnoli, T. Yasa, G. Paniagua, S. Duni, and L. Castillon. Aerodynamic analysis of an innovative low pressure vane placed in a s-shape duct. *Journal of Turbomachinery, 134(1), May, p. 13*, 2011.

D. Lengani, C. Santner, R. Spataro, B. Paradiso, and E. Göttlich. Experimental investigation of the unsteady flow field downstream of a counter-rotating two-spool turbine rig. *Proceedings of ASME Turbo Expo, 2012*, 2012. GT2012-68583.

A. Marn. On the aerodynamics of aggressive intermediate turbine ducts for competitive and environmentally friendly jet engines. *PhD thesis, Institute for Thermal Turbomachinery and Machine Dynamics of Graz University of Technology*, 2008. ISBN 0:978-91-7385-264-7.

F. R. Menter. Two-equation eddy-viscosity turbulence models for engineering applications. *AIAA Journal*, 32(8):1598–1605, 1994.

R. J. Miller, R. W. Moss, R. W. Ainsworth, and N. W. Harvey. The development of turbine exit flow in a swan-necked inter-stage diffuser. *In Proceedings of ASME Turbo Expo 2003, June 16-19, Atlanta, Georgia, USA*, 2003. GT2003-38174.

R. Pecnik, P. Pieringer, and W. Sanz. Numerical investigation of the secondary flow of a transonic turbine stage using various turbulence closures. *Proceedings of ASME Turbo Expo 2005, Reno-Tahoe, Nevada, USA*, 2005. GT2005-68754.

G. Pullan, J. Denton, and M. Dunkley. An experimental and computational study of the formation of a streamwise shed vortex in a turbine stage. *Journal of Turbomachinery, 125, April, pp. 291–297*, 2003.

G. Pullan, J. Denton, and E. Curtis. Improving the performance of a turbine with low aspect ratio stators by aft-loading. *Journal of Turbomachinery. 2006. Vol. 128(3). pp. 492–499*, 2006.

P. L. Roe. Approximate riemann solver, parameter vectors and differencing scheme. *Journal of Computational Physics. Vol 43. pp. 357–372*, 1981.

C. Santner, B. Paradiso, F. Malzacher, M. Hoeger, J. Hubinka, and E. Göttlich. Evolution of the flow through a turning mid turbine frame applied between a transonic hp turbine stage and a counter-rotating LP turbine. *Proceedings of 9^{th} European Turbomachinery Conference, Istanbul, Turkey, Paper No. 110*, 2011.

R. Spataro, C. Santner, D. Lengani, and E. Göttlich. On the flow evolution through a LP turbine with wide-chord vanes in an s-shaped channel. *Proceedings of ASME 2012 TURBO EXPO, Copenhagen, Denmark*, 2012. GT2012-68178.

R. Spataro, E. Göttlich, D. Lengani, C. Faustmann, and F. Heitmeir. Developement of a turning mid turbine frame with embedded design - part I: Design and steady measurements. *In Proceedings of ASME 2013 Turbo EXPO, June 3-7, San Antonio Convention Center, San Antonio, Texas, USA*, 2013a. GT2013-95279.

R. Spataro, E. Göttlich, D. Lengani, C. Faustmann, and F. Heitmeir. Developement of a turning mid turbine frame with embedded design - part II: Unsteady measurements. *Proceedings of ASME 2013 Turbo EXPO, San Antonio, Texas, USA*, 2013b. GT2013-95280.

J. M. Tyler and T. G. Sofrin. Axial flow compressor noise studies. *SAE Transaction, Vol. 70, pp. 309–332.*, 1962.